

Extreme multiplicity in cylindrical Rayleigh-Bénard convection:

I. Time-dependence and oscillations

Katarzyna Borońska^{1,*} and Laurette S. Tuckerman^{1,†}

¹ *Laboratoire d'Informatique pour la Mécanique et les Sciences de l'Ingénieur (LIMSI-CNRS), B.P. 133, 91403 Orsay, France*
(Dated: May 30, 2019)

Motivated by the results of Hof et al. [*Phys. Fluids* **11**, 2815–2817 (1999)], who observed coexistence of several stable states at the same parameter values, we have carried out simulations at the same Prandtl number and aspect ratio. We have used two kinds of thermal boundary conditions: perfectly insulating sidewalls and perfectly conducting sidewalls. For both cases we obtain a wide variety of coexisting steady and time-dependent flows.

PACS numbers: 47.20.Ky, 47.20.Bp, 47.10.Fg, 47.11.Kb

I. INTRODUCTION

The flow patterns realized by Rayleigh-Bénard convection depend not only on the fluid parameters and container geometry, but also on the flow history. This was strikingly illustrated by the experimental study carried out by Hof *et al.* [1, 2]. They investigated a cylinder of small aspect ratio $\Gamma \equiv \text{radius/height} = 2.0$ filled with water (Prandtl number 6.7). Varying the Rayleigh number through different sequences of values, they obtained several different stable patterns for the same final Rayleigh number. For 14 200 they observed two, three and four parallel rolls, a “mercedes” pattern with three spokes of ascending or descending fluid and even an axisymmetric state (figure 1). They also reported a transition from an axisymmetric steady state towards azimuthal waves.

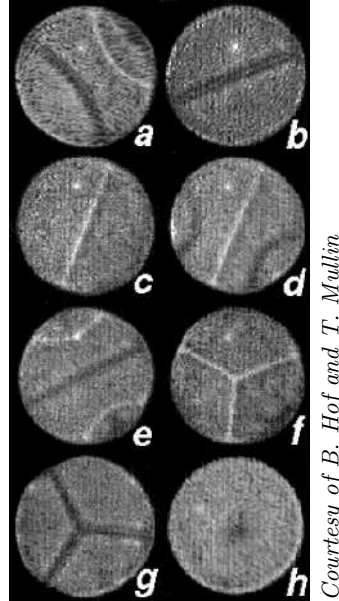


FIG. 1: Patterns observed in the experiment of Hof *et al.*: (a) three rolls, (b) two rolls, (c) inverted two rolls, (d) four rolls, (e) inverted four rolls, (f) mercedes, (g) inverted mercedes, (h) axisymmetric pattern. Dark areas correspond to hot (rising) and bright to cold (descending) fluid.

*k.boronska@leeds.ac.uk; www.comp.leeds.ac.uk/kb

†laurette@pmmh.espci.fr; www.pmmh.espci.fr/~laurette

We begin by reviewing the literature on Rayleigh-Bénard convection in cylinders with small-to-moderate aspect ratio $1 \lesssim \Gamma \lesssim 10$. Our interest in such geometries stems from the fact that they are the battleground of two competing tendencies, over an appreciable Rayleigh-number range. At threshold, the patterns necessarily resemble eigenmodes of the Laplacian, i.e. they are trigonometric in the azimuthal angle. But at higher Ra , the patterns form rolls, bending and pinching so as to fit into the cylinder.

The stability of the conductive state in a cylindrical geometry was well established in the 1970s–1980s [3, 4, 5, 6]. Critical Rayleigh numbers Ra_c are about 2000 for $\Gamma \sim 1$, increasing steeply for lower Γ and decreasing asymptotically towards $Ra_c = 1708$ for $\Gamma \rightarrow \infty$. The seminal paper of Buell and Catton [6] surveyed the influence of sidewall conductivity on the onset of convection by performing linear analysis for the aspect ratio range $0 < \Gamma \leq 4$. They determined the critical Rayleigh number and azimuthal wavenumber as a function of both aspect ratio and sidewall conductivity, thus completing the results of the previous investigations, which considered either perfectly insulating or perfectly conducting walls. The flow succeeding the conductive state is three-dimensional over large ranges of aspect ratios, contrary to the expectations of Koschmieder [7]. Similar calculations were carried out by Marques *et al.* [8].

The stability of the first convective state, for situations in which the primary flow is axisymmetric, was investigated in the 1980s–1990s [9, 10, 11, 12] for a variety of aspect ratios and Prandtl numbers. Bifurcation-theoretic scenarios for axisymmetric flows have been investigated by Barkley and Tuckerman [13] and Siggers [14]. Experiments on the competition between various convective patterns in a constrained cylindrical geometry ($\Gamma \approx 7.5$) were carried out during this period [15, 16, 17] and the dynamics interpreted in terms of the instabilities of two-dimensional straight rolls [18].

Several time-dependent simulations since 2000 have focused on the variety of coexisting non-axisymmetric patterns for $\Gamma \approx 4$. Rüdiger and Feudel [19] used a spectral simulation to investigate the aspect ratio $\Gamma = 4$, finding the stability ranges of several patterns – parallel rolls, target and spirals – with overlapping stability ranges in Rayleigh number. Paul *et al.* [21] studied the dislocation dynamics of curved rolls near onset.

Several studies have focused on configurations similar or identical to that of Hof *et al.* [1]. Leong [20] used a finite difference method to simulate convective flows for Prandtl number $Pr = 7$ in cylinders of aspect ratios $\Gamma = 2$ and 4 and adiabatic lateral walls and observed several steady patterns – parallel rolls, three-spoke flow and axisymmetric state – all of which were stable in the range $6250 \leq Ra \leq 37\,500$. Ma *et al.* [22] used a finite volume method to simulate the parameters $\Gamma = 2$ and $Pr = 6.7$ of Hof *et al.* [1]. As in our prior study [23], they used time-dependent simulation at $Ra = 14\,200$ to reproduce the five states of Hof *et al.* They also calculated the first nine primary bifurcations to modes of varying azimuthal wavenumbers, and several secondary bifurcations, all taking place for $Ra \leq 2500$. However, they reported no results for Ra between 2500 and 14 200, nor for any values above 14 200.

The work we present here is based on that of Borońska [23] and covers simulations of $\Gamma = 2$ and $Pr = 6.7$ over the entire Rayleigh-number range up to 30 000. We carry out a complete survey of the convective patterns we locate; we then carry out the same study for the case of conductive sidewalls. A companion paper [24] takes the present article as a starting point to compute a bifurcation diagram for the insulating sidewall case in the range $Ra \leq 30\,000$ which connects the patterns at $Ra = 14\,200$ with the primary bifurcations from the conductive branch.

II. GOVERNING EQUATIONS AND NUMERICAL METHODS

The methods used in our study are described in this section. We first present the nonlinear equations governing the system. We then describe the most important aspects of the numerical methods used for integrating the differential equations. A detailed description of all numerical techniques used can be found in Tuckerman [25].

A. Equations and boundary conditions

We consider a fluid confined in a cylinder of depth d and radius R , whose aspect ratio is defined as $\Gamma \equiv R/d$ (figure 2). The fluid has kinematic viscosity ν , density ρ , thermal diffusivity κ and thermal expansion coefficient (at constant pressure) γ . The top and bottom temperatures of the cylinder are kept constant, at $T_0 - \Delta T/2$ and $T_0 + \Delta T/2$, respectively. The Rayleigh number Ra and the Prandtl number Pr are defined by

$$Ra \equiv \frac{\Delta T g \gamma d^3}{\kappa \nu}, \quad Pr \equiv \frac{\nu}{\kappa}. \quad (1)$$

Using the units d^2/κ , d , κ/d and $\nu\kappa/\gamma g d^3$ for time, distance, velocity and temperature, and defining H to be the dimensionless temperature deviation from the linear vertical profile, we obtain the Navier–Stokes and Boussinesq

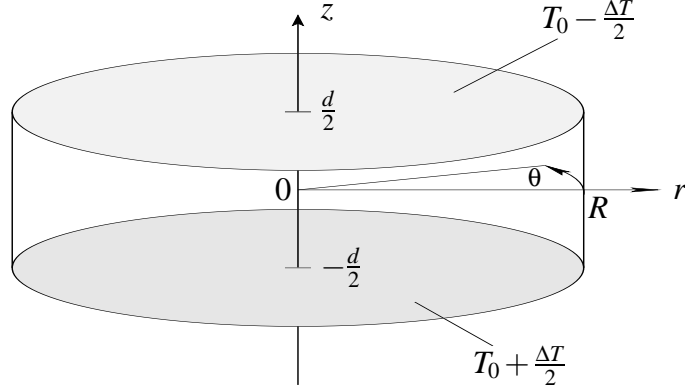


FIG. 2: Geometry and coordinate system.

dimensionless equations governing the system:

$$\partial_t H + (\mathbf{U} \cdot \nabla) H = Ra U_z + \nabla^2 H \quad (2a)$$

$$Pr^{-1} (\partial_t \mathbf{U} + (\mathbf{U} \cdot \nabla) \mathbf{U}) = -\nabla P + \nabla^2 \mathbf{U} + H \mathbf{e}_z \quad (2b)$$

$$\nabla \cdot \mathbf{U} = 0. \quad (2c)$$

We used realistic boundary conditions for the velocity, with no-penetration and no-slip on the horizontal plates and sidewalls:

$$\mathbf{U} = 0 \quad \text{for } z = \pm 1/2 \quad \text{or } r = \Gamma. \quad (3a)$$

We assume that perfectly conducting horizontal plates maintain the temperature constant (homogeneous Dirichlet condition for H)

$$H = 0 \quad \text{for } z = \pm 1/2. \quad (3b)$$

The sidewalls are either perfectly insulating (Neumann boundary conditions)

$$\partial_r H = 0 \quad \text{for } r = \Gamma. \quad (3c)$$

or perfectly conducting, so that a linear vertical temperature profile is maintained within them (Dirichlet boundary conditions)

$$H = 0 \quad \text{for } r = \Gamma. \quad (3d)$$

The code has also a possibility we have not utilized here, of interpolating between these two conditions in order to represent sidewalls with finite values of conductivity, as was done in [13]:

$$\mu_{Dir} H + \mu_{Neu} \partial_r H = 0 \quad \text{for } r = \Gamma. \quad (4)$$

B. Spatial and temporal discretization

We represent the fields by a tensor product of trigonometric functions in θ and Chebyshev polynomials on the intervals $-1/2 \leq z \leq 1/2$ and $0 \leq r \leq \Gamma$. A representation which is regular at the origin can be created by imposing parity restrictions on the Chebyshev and Fourier functions [25]. The temperature and vertical velocity are approximated by the formula

$$f(r, \theta, z) = \sum_{m=0}^{N_\theta/2} \sum_{\substack{j \geq m \\ j+m \text{ even}}}^{2N_r-1} \sum_{k=0}^{N_z-1} \hat{f}_{j,m,k} T_j(r/\Gamma) T_k(2z) e^{im\theta} + \text{c.c.} \quad (5)$$

For the radial and azimuthal velocity components, the same representation is used, except with $j+m$ odd. In the code, less stringent parity rules are used, ensuring only that the first three derivatives of f are continuous at the cylinder axis. The pseudospectral method [26] calls for carrying out differentiation on the spectral representation on the right-hand-side of (5). Multiplication is carried out by first transforming to a representation on a Gauss-Lobatto grid, which includes the boundary points. The Fourier transforms, including cosine transforms for the Chebyshev polynomials, use the Temperton algorithms [27] for dimensions which are not powers of two. Radial and axial boundary conditions are imposed via the tau method, i.e. replacing the equations corresponding to the highest order Chebyshev polynomials by the boundary conditions.

The temporal discretization is semi-implicit. The viscous, diffusive, and buoyancy terms are integrated via the backwards Euler scheme while the advective terms are integrated via the Adams–Bashforth scheme. Applying these formulas to (2a)-(2b), we obtain:

$$(1 - \Delta t \nabla^2) H^{n+1} = H^n + \frac{\Delta t}{2} [-3(\mathbf{U}^n \cdot \nabla) H^n + (\mathbf{U}^{n-1} \cdot \nabla) H^{n-1} + Ra(3U_z^n - U_z^{n-1})] \quad (6a)$$

$$(1 - \Delta t Pr \nabla^2) \mathbf{U}^{n+1} + \Delta t Pr \nabla P^{n+1} = \mathbf{U}^n + \frac{\Delta t}{2} [-3(\mathbf{U}^n \cdot \nabla) \mathbf{U}^n + (\mathbf{U}^{n-1} \cdot \nabla) \mathbf{U}^{n-1}] + \Delta t Pr H^{n+1} \mathbf{e}_z. \quad (6b)$$

In the Helmholtz operators on the left-hand-sides of (6), each Fourier mode m in the representation (5) is decoupled from the other Fourier modes. In addition to this economy, for each m , the matrix representing a differential operator can be diagonalized in the z direction [28] and reduced to a banded matrix in the r direction [29]. The storage and the time for inversion of the resulting linear systems is then on the order of $N_\theta N_r N_z^2$.

C. Resolution

In order to choose our spatial resolution we carried out several runs at varying resolution at Rayleigh number 14 000 and timestep $\Delta t = 2 \times 10^{-4}$, comparing the evolution of several quantities, such as temperature and velocity at fixed gridpoints, several spectral coefficients and the total energy

$$E \equiv \frac{1}{Ra} \left(\frac{1}{Pr} \int_{\text{vol}} \mathbf{U} \cdot \mathbf{U} + \frac{1}{Ra} \int_{\text{vol}} H^2 \right). \quad (7)$$

The resolution $N_r \times N_\theta \times N_z = 40 \times 120 \times 20$ was chosen as a compromise between accuracy and efficiency. This resolution insured that the spectral coefficients decayed exponentially with wavenumber or Chebyshev index. We also reproduced a few high Rayleigh number states ($20\,000 \leq Ra \leq 30\,000$) at the higher resolution $N_r \times N_\theta \times N_z = 60 \times 160 \times 30$. In case of any uncertainty concerning the resulting pattern, the mesh was refined; each such test confirmed the results obtained with the previous resolution.

The timestep Δt chosen depends on Rayleigh number and on the evolution of the system. For higher Rayleigh numbers and abrupt transitions, a smaller timestep is required. For slowly evolving fields, the number of iterations necessary for convergence becomes too great, unless we use larger Δt . We chose the initial timesteps as a function of Rayleigh number and if the evolution slowed down, we continued the simulation with an increased Δt . The timesteps we used varied from $\Delta t = 8 \times 10^{-4}$ for $Ra = 2000$ to $\Delta t = 2 \times 10^{-4}$ for $Ra = 30\,000$. The timestep was reduced when necessary, especially when any oscillations appeared.

D. Incompressibility: velocity–pressure decoupling

In order to decouple velocity and pressure, the divergence operator is applied to (6b) to derive a Poisson equation for P

$$\nabla^2 P = \nabla \cdot \left(\frac{1}{2 Pr} [-3(\mathbf{U}^n \cdot \nabla) \mathbf{U}^n + (\mathbf{U}^{n-1} \cdot \nabla) \mathbf{U}^{n-1}] + H^{n+1} \mathbf{e}_z \right), \quad (8)$$

where $\nabla \cdot \mathbf{U}^n = \nabla \cdot \mathbf{U}^{n+1} = 0$ and $\nabla \cdot \nabla^2 = \nabla^2 \nabla \cdot$ have been used.

The thorny issue of boundary conditions for this Poisson equation can be addressed in several ways [25, 30]. Most approaches derive boundary conditions for P from the original momentum equation (2b). This will yield a divergence which is proportional to some power of Δt . This is usually acceptable for time integration, where Δt is small.

However, to carry out Newton's method for steady state solving, as we will do in our companion paper [24], we adapt this time-stepping code, using $\Delta t \gg 1$. We therefore require a method which imposes incompressibility regardless of Δt . Essentially, the correct boundary condition for (8) is

$$\nabla \cdot \mathbf{U} = 0 \quad \text{for } z = \pm 1/2 \quad \text{or} \quad r = \Gamma, \quad (9)$$

which again couples velocity and pressure.

We use a Green's function or influence matrix method [25] as follows.

In a preprocessing step, we calculate a set of *homogeneous* solutions $\mathbf{U}^{\text{hom},j}$:

- (h,i) We solve the homogeneous version of the pressure Poisson equation (8) with all possible Dirichlet boundary conditions, for example, by choosing each point \mathbf{x}_j on the boundary in turn and setting the boundary conditions to be 1 at \mathbf{x}_j and 0 elsewhere. (An equivalent approach would loop over all of the highest Chebyshev components.) This yields a set of homogeneous pressure solutions $P^{\text{hom},j}$.
- (h,ii) We then solve the homogeneous version of (6b), i.e. setting the right-hand-side to zero, setting $P = P^{\text{hom},j}$ and imposing the homogeneous boundary conditions (3). This yields a set of homogeneous velocity solutions $\mathbf{U}^{\text{hom},j}$.
- (h,iii) We complete the preprocessing step by calculating $\mathcal{C}_{ij} \equiv \nabla \cdot \mathbf{U}^{\text{hom},j}(\mathbf{x}_i)$ on all points \mathbf{x}_i of the boundary. \mathcal{C} is the influence (or capacitance) matrix.

At each timestep, we calculate a *particular* solution \mathbf{U}^{part} and then the final solution \mathbf{U} as follows:

- (p,i) We solve the pressure Poisson equation (8) with the non-zero right-hand-side in (8), but with homogeneous Dirichlet boundary conditions. This yields the particular pressure P^{part} .
- (p,ii) We solve (6b) for the velocity, using $P = P^{\text{part}}$ and imposing the homogeneous boundary conditions (3). This yields the particular velocity \mathbf{U}^{part} .
- (p,iii) We calculate $\nabla \cdot \mathbf{U}^{\text{part}}(\mathbf{x}_i)$, the divergence of the particular velocity on each point on the boundary.
- (p,iv) By solving the linear system

$$0 = \nabla \cdot \mathbf{U}^{\text{part}}(\mathbf{x}_i) + \sum_j c_j \nabla \cdot \mathbf{U}^{\text{hom},j}(\mathbf{x}_i) \quad (10)$$

involving the influence matrix, we determine the coefficients c_j .

- (p,v) The final solution is assembled as

$$\mathbf{U}^{n+1} = \mathbf{U}^{\text{part}} + \sum_j c_j \mathbf{U}^{\text{hom},j}. \quad (11)$$

Alternatively, if the homogeneous solutions $\mathbf{U}^{\text{hom},j}$ are not stored, we obtain the final solution by repeating steps (p,i) and (p,ii), but using the coefficients c_j as inhomogeneous Dirichlet boundary conditions for P .

We point out several final aspects of this influence matrix method:

- As mentioned previously, the differential operators are decoupled by azimuthal Fourier mode; this also applies to the influence matrix, making its size manageable, i.e. $(2N_r + N_z) \times (2N_r + N_z)$ for each m .
- Because the system (10) is in fact overdetermined, the influence matrix must be regularized (e.g. zero eigenvalues replaced by finite values) in order to be inverted.
- Although $\nabla \cdot$ and ∇^2 commute, even for the discretized operators, this is no longer the case when boundary conditions are substituted for the highest order equations, essentially because differentiation lowers the polynomial order. The *tau correction* keeps track of the derivatives of the dropped frequencies, and, once the solution is obtained, the necessary correction is applied to it. In the code, the tau correction is implemented, together with the boundary conditions, in the influence matrix.

E. Computing details

We used a simulation code written in Fortran in 1980s [25], slightly modernized and optimized for vector platforms NEC SX-5 and NEC SX-8. The Fourier transforms used to convert from the spectral to the physical representation (in which the nonlinear term is computed at each timestep) were carried out by the NEC emulation of the SciLib Cray library. A typical three-dimensional nonlinear run of 1000 timesteps required 70 CPU seconds. Patterns were visualized using the VTK library. The color map we used is based on CMRmap [31], in which luminosity changes monotonically. Thus visualizations are correctly rendered in greyscale as well as in color.

III. RESULTS

A. Insulating sidewalls

In their experiment, Hof *et al.* [1] produced a large number of convective patterns by increasing and decreasing the Rayleigh number in a variety of ways. We have performed a sequence of simulations, varying the initial state and the Rayleigh number, in order to find the asymptotic state for each configuration. We chose to use Neumann boundary conditions for the temperature deviation on the sidewalls, which corresponds to perfect insulation. This should be close to the experimental setup, where Perspex plexiglass (a poor thermal conductor) was used. Rather than filling in the whole table of combinations of Rayleigh numbers and initial conditions, we attempted to probe this space, concentrating in particular on obtaining patterns resembling those of Hof at $Ra = 14\,200$, for which they observed five different steady patterns.

1. Experimental and numerical protocol

We initialized the simulations with a slightly perturbed conductive solution. This can be seen as corresponding to a sudden jump of heating power in an experimental setup, where previously a fluid was maintained below the convection threshold. Such simulations gave us different patterns, depending on Rayleigh number. Once we obtained these stable convective flows, we used them as initial states at other Rayleigh numbers. This is again comparable to an experimental situation in which, once a pattern is stabilized, the heating power is changed abruptly.

In order to qualify a solution as stable, we monitored the evolution of the flow structure, its energy and the azimuthal velocity at two arbitrarily chosen points. We qualified a state as stable if the observed quantities did not change more than about 0.1% and seemed to saturate. We were especially careful about classifying as stable a state we qualified already as transitional for another Rayleigh number. We cannot, however, completely exclude the possibility that a long-lasting transitional state was interpreted as stable.

The field visualized throughout this article is the temperature deviation from the basic vertical profile, referred to merely as the temperature, as for fixed z they differ only by a constant. The horizontal cuts are taken in the midplane; dark (bright) areas indicate hot (cold) zones. The time is expressed in dimensionless units of the vertical thermal diffusion time $[t] = d^2/\kappa$.

The patterns we observed and the transitions between them are described in the sections which follow. In order to orient the reader, we anticipate these results and present on figure 3 a schematic diagram of the stable patterns we observed for different Rayleigh numbers. More quantitative diagrams can be found at the end of section III A.

2. Evolution from perturbed conductive state

We first report the results obtained from the slightly perturbed conductive solution, shown in figure 4a). We run a series of simulations for Rayleigh numbers between 1600 and 23 000. Depending on the Rayleigh number, this state evolves towards different flows shown on figure 4b-e.

For $Ra \lesssim 1900$, the initial perturbation decays to zero, i.e. the conductive state. For Ra near 2000, the final state is a quadrupole pattern which we will call the *pizza state* (shown on figure 4b). This state has four well-separated sections, resembling pieces of a pizza. Each section has either a hot round spot in the center with colder area along the sidewall, or a cold round spot in the center with warmer area at the sidewall.

For Ra between 3000 and 20 000, the system evolves towards states with parallel or rather quasi-parallel rolls (see figure 4c,d): below 10 000 the final state is a four-roll pattern and for 10 000 and above, the final solution is a three-roll

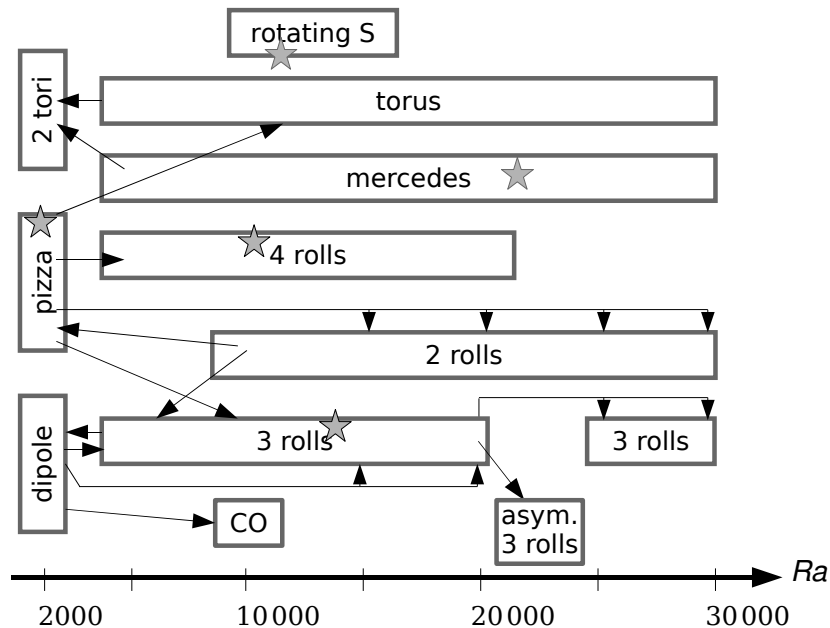


FIG. 3: Schematic diagram of stability ranges and transitions between convective patterns as a function of Rayleigh number for $\Gamma = 2$, $Pr = 6.7$ and insulating sidewalls. Stars denote solutions obtained from a slight perturbation of the conductive state, at given Ra (see figure 4).

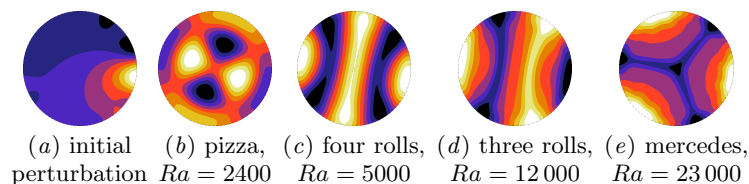


FIG. 4: Initial perturbation and convective patterns obtained from perturbed conductive state at different Rayleigh numbers. Visualization of the temperature in the cylinder's midplane, dark: hot/ascending, bright: cold/descending fluid.

state. Finally, for $Ra \approx 23000$, the final pattern consists of three radial spokes of cold descending fluid, named the *mercedes* pattern by Hof [2] (figure 4e). For all these patterns, the roll boundaries become thinner as the Rayleigh number is increased.

3. Three-roll patterns

In the second series of simulations, we used as the initial condition the three-roll state previously converged at $Ra = 14200$, like that in figure 4d. Below the critical Rayleigh number this pattern decays to zero via an intermediate *dipole pattern* and for $Ra = 2000$ the three rolls transform into a dipole state, as shown on figure 5. The dipole pattern (c) resembles an $m = 1$ azimuthal mode.

For $Ra = 5000$ and above, up to $Ra = 33000$, the three-roll state remains stable, with the rolls more curved for higher Rayleigh numbers (see figure 6). An exception is the range between $Ra = 20000$ and $Ra = 25000$, where this pattern becomes asymmetric – the band of colder fluid between the central roll and the left roll moves slightly towards the center as the Rayleigh number is increased (see figure 7). This is similar to the results of Hof *et al.* [1], although they found that the leftmost roll vanishes eventually at $Ra = 21000$, where the flow forms a two-roll pattern. Figure 8 shows the Rayleigh-number dependence of the temperature at a fixed point and of the energy; both show deviations in the range $20000 < Ra < 25000$. We conclude that a bifurcation is present. In the experiment this evolution yielded a two-roll pattern and, during our further analysis of two-roll states, we found that their energy indeed approaches that of shifted (asymmetric) three rolls.

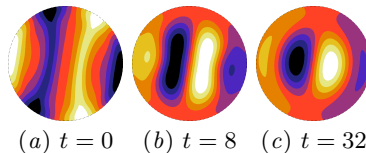


FIG. 5: Evolution of the convective pattern at $Ra = 2000$ for a simulation initialized with a three-roll pattern.

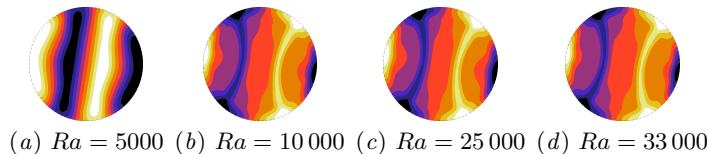


FIG. 6: Three-roll patterns converged at different Rayleigh numbers.

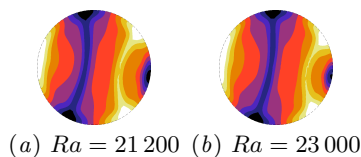


FIG. 7: Asymmetric three-roll pattern with central roll shifted to the right, obtained for Ra between 20 000 and 25 000.

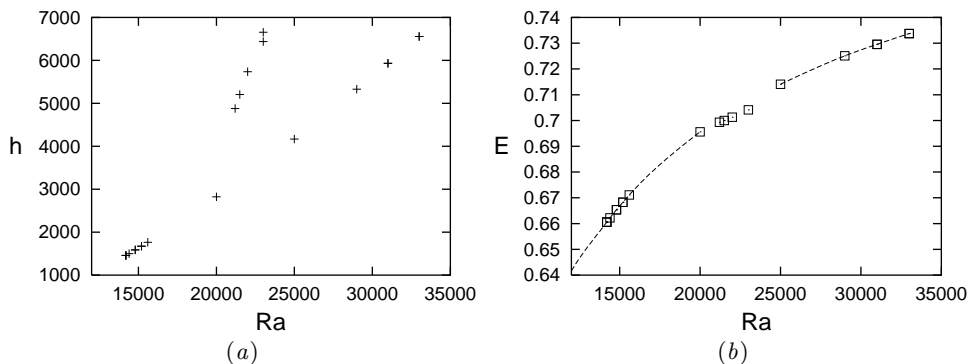


FIG. 8: Dependence of the three-roll patterns on Rayleigh number: (a) temperature at $r = 0.3$, $z = 0.25$, $\theta = 0$; (b) energy.

4. Evolution from four rolls

We used a four-roll pattern converged at $Ra = 3000$, like that in figure 4c as an initial condition for simulations at $4000 \leq Ra \leq 20\,000$. The newly evolved patterns are also of the four-roll family, and, as in the case of three rolls, the roll boundaries become thinner as the Rayleigh number is increased (see figure 9). We then used the four-roll state converged for $Ra = 20\,000$ depicted in figure 9c as an initial condition at Rayleigh numbers 25 000 and 29 000. This time the geometry of the pattern changes, as displayed on figure 10 – the four-roll pattern turns into a *cross pattern* with four spokes of descending cold fluid. The cross flow does not saturate in the time during which we observed it, but continues to evolve slowly; we suspect that it is a transitional rather than an asymptotic state. This would be in agreement with Hof [32], who observed that the cross pattern is a long-lasting transient state unstable to a mercedes pattern.

5. Evolution from pizza pattern

We used the pizza pattern at $Ra = 2000$, like that in figure 4b, as an initial condition for a series of simulations at several Rayleigh numbers between 5000 and 29 000. In this range the pizza pattern is not stable. For $Ra = 5000$

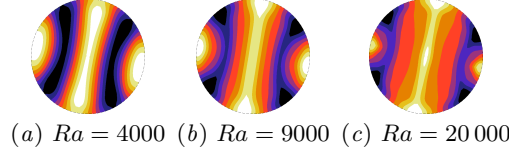


FIG. 9: Four-roll patterns for different Rayleigh numbers.

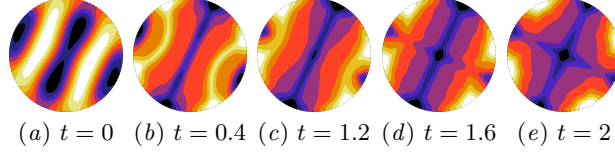


FIG. 10: Evolution of the four-roll pattern towards (probably transitional) cross pattern at $Ra = 25\,000$.

it changes into four rolls (see figure 11) and for $Ra = 10\,000$ into three rolls (figure 12). For $Ra = 14\,200$ the initial pizza flow evolves into a *torus pattern* – an axisymmetric state with one toroidal roll, passing through an intermediate *eight pattern*. This evolution is displayed on figure 13. The transitional eight pattern was also observed by Hof [32].

For $Ra \geq 15\,000$ the pizza state, after passing through a series of various transitional patterns, eventually evolves to a two-roll flow. Figure 14 displays the evolution of the system for $Ra = 16\,000$, where we describe the intermediate states as: *triangle mosaic* (b), *eye* (d) and *imperfect eight* (f). Figure 15 presents the system behaviour for $Ra = 29\,000$, where the intermediate patterns between pizza and two rolls are *six-spoke elongated-star* (d) and *six-spoke star* (e).

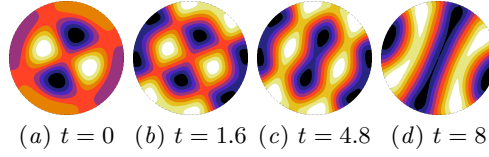


FIG. 11: Evolution from pizza pattern at $Ra = 5000$.

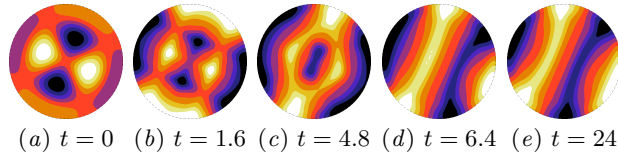


FIG. 12: Evolution from pizza pattern at $Ra = 10\,000$.

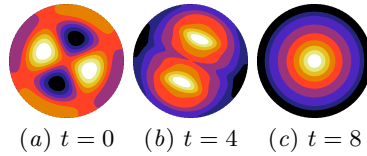


FIG. 13: Evolution of pattern at $Ra = 14\,200$: from initial pizza through eight towards final torus pattern.

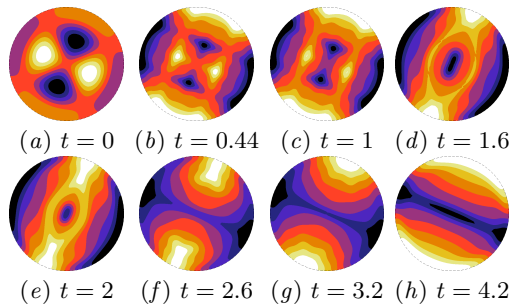


FIG. 14: Evolution of pattern at $Ra = 16\,000$ from initial pizza through a series of intermediate states towards the final two-roll pattern.

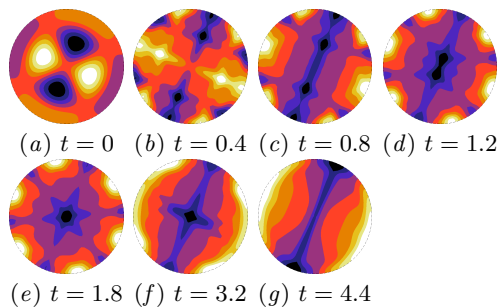


FIG. 15: Evolution of pattern at $Ra = 29\,000$ from initial pizza through a series of intermediate states towards the final two-roll pattern.

6. Evolution from two rolls

Another initial condition we used was the two-roll state like that in figure 14h, converged previously at $Ra = 15\,000$. For $Ra = 2000$ it leads to the pizza pattern, and for $Ra = 5000$ a three-roll state. For $10\,000 \leq Ra < 29\,000$, we found the two roll pattern to be stable. At $Ra = 29\,000$ the roll boundaries start oscillating slightly. Figure 16 presents two-roll flow visualizations for different Rayleigh numbers.

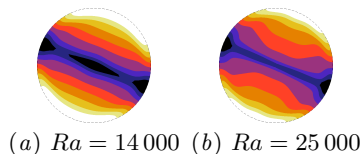


FIG. 16: Two-roll pattern at different Rayleigh numbers.

7. Axisymmetric flows

The axisymmetric pattern, shown in figure 13c and used as an initial condition, also leads to axisymmetric patterns for a wide range of Rayleigh numbers $2000 \leq Ra \leq 33\,000$ (see figure 17). For $Ra = 2000$ there are two concentric toroidal rolls instead of one. This is in partial agreement with Hof [2], who found toroidal flow to be stable for $Ra > 3500$, but to evolve towards a rotating three-petaled pattern for $Ra \gtrsim 23\,000$. At these values of Ra , our simulations still converge towards a stationary axisymmetric flow, although in an oscillatory manner. All axisymmetric patterns we observed were truly two-dimensional, with no azimuthal velocity.

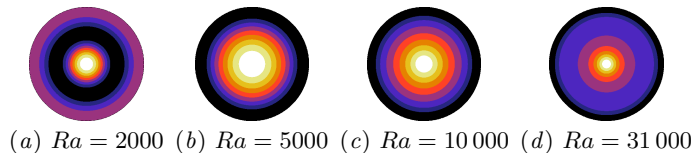


FIG. 17: Axisymmetric patterns at different Rayleigh numbers.

8. Evolution from mercedes pattern

We ran a series of simulations using as the initial condition the mercedes pattern of figure 4e. For every Rayleigh number in the range $5000 \leq Ra \leq 29\,000$ this gave stable mercedes patterns and for $Ra = 2000$ it evolves to a two-roll axisymmetric pattern. Figure 18 displays the final patterns for different Rayleigh numbers.

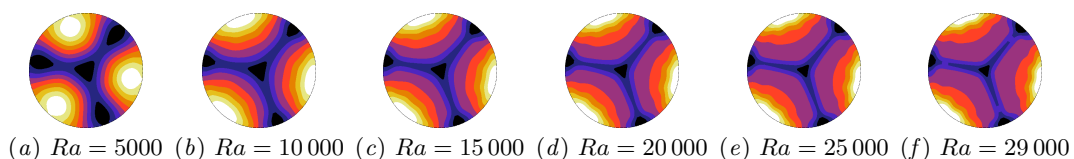
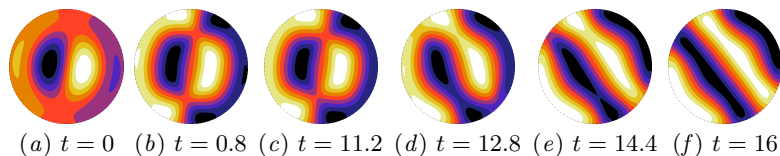
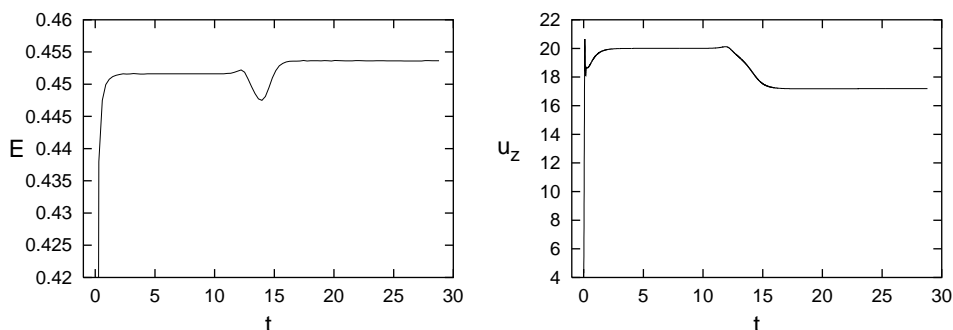


FIG. 18: Mercedes patterns at different Rayleigh numbers.

9. Evolution from dipole pattern

Another initial condition we used was the dipole pattern shown in figure 5c. For Rayleigh numbers between 5000 and 29 000, with the exception of 10 000, the flow evolves towards a three-roll pattern. The evolution of the flow at $Ra = 5000$ is presented on figures 19 and 20. At this Rayleigh number the system passes through a long-lasting intermediate *dipole smile state* (figure 19c), whose lifetime is of order 10. The flow patterns appearing for

FIG. 19: Evolution from dipole pattern at $Ra = 5000$.FIG. 20: Evolution from the dipole pattern at $Ra = 5000$: (a) energy, (b) vertical velocity at one point. A long-lasting transient state is visible between $t = 3$ and $t = 12$.

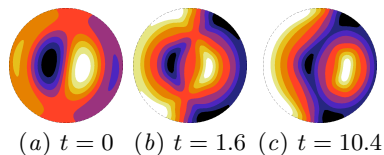


FIG. 21: Evolution from dipole pattern through dipole smile into final CO pattern at $Ra = 10\,000$.

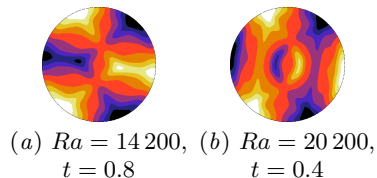


FIG. 22: Transitional patterns observed during evolution from dipole into three-roll pattern.

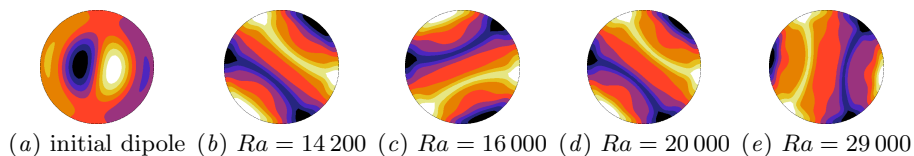


FIG. 23: Initial dipole (a) and final patterns for various Rayleigh numbers.

$Ra = 10\,000$ are depicted on figure 21. An intermediate dipole smile state appears also (21b), with a lifetime of about 2. The final solution is a *CO pattern* (21c), composed of one curved and one circular roll. This state resembles the three-roll pattern with the ends of two neighbouring rolls joined together, but its energy is higher than that of the three-roll state at the same Ra . At higher Rayleigh numbers, where the asymptotic solution is again three-roll flow, transitional patterns also appear (figure 22). The final patterns are shown on figure 23, with the initial dipole pattern for comparison. The initial pattern orientation does not seem to determine the direction of the rolls of the final pattern. Figure 24 depicts the energy of patterns evolved starting from a dipole pattern as a function of Rayleigh number. For comparison, the energy of three-roll states from section III A 3 is also displayed. They are in perfect agreement with the sole exception of $Ra = 10\,000$: the energy of the CO state is lower.

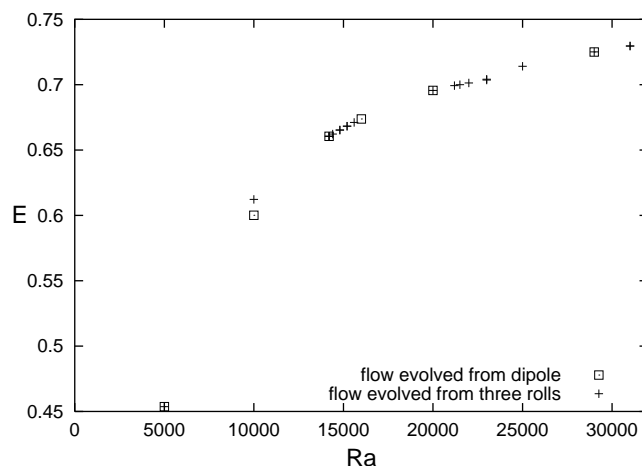


FIG. 24: Squares: energy of the flow evolved from dipole state as a function of Rayleigh number; crosses: energy of the flow evolved from three-roll state (for comparison). At $Ra = 10\,000$ the dipole pattern evolves into a CO pattern.

10. Dipole-shaped perturbation

As in section III A 2, we again used as an initial condition a low-amplitude state. This initial condition was obtained as follows. We began with the three-roll state converged at $Ra = 14\,200$, and lowered Ra to 1200, i.e. below the convective threshold. A transient dipole appeared, similar to that depicted in figure 5c, and we halted the evolution before the flow reverted to the conductive state. Although this initial condition is not a converged pattern, it occurs during the evolution of the system, and is thus reachable experimentally.

Starting with this initial condition, simulation yields a dipole at $Ra = 2000$ and three rolls at $Ra = 5000$. However, for $10\,000 \leq Ra \leq 15\,000$, we obtain a new state. A transitional dipole smile gives way to a slowly rotating roll in the shape of the letter S, which we will refer to as a *rotating S pattern*. A visualization of this time-dependent state at different times is displayed on figure 25 and the evolution of the temperature at two points is plotted in figure 26. The rotation is very slow: one period is of the order of ten, and the frequency grows with the Rayleigh number. Figure 27 shows the dependence of the frequency and energy of the rotating S on Rayleigh number.

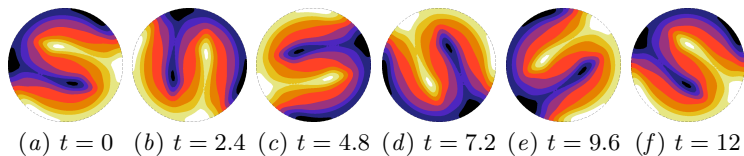


FIG. 25: Rotating S pattern at $Ra = 12\,500$ at six different times.

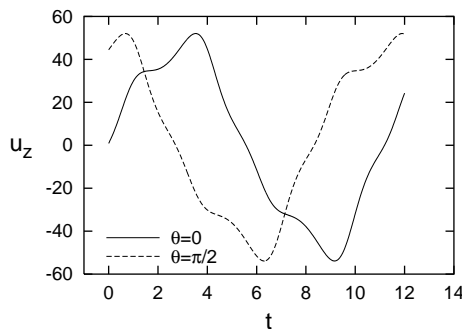


FIG. 26: Evolution of vertical velocity in time for rotating S pattern at two points of the same r and z and different θ .

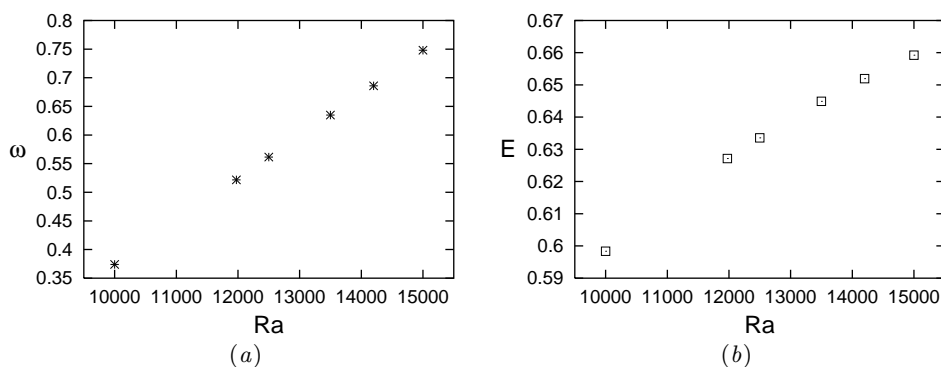


FIG. 27: Frequency and energy of the rotating S pattern as a function of Rayleigh number.

The evolution of the dipole pattern at $Ra = 16\,000$ is shown on figure 28. It passes through an intermediate *three-part dipole pattern* before finally becoming a dipole-smile pattern. This pattern, observed for $5000 \leq Ra \leq 15\,000$ as a transient pattern, seems to be stable for this Rayleigh number.

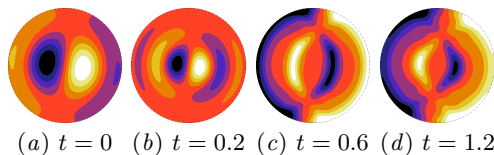


FIG. 28: Evolution from dipole-shaped perturbation into a stable dipole smile pattern at $Ra = 16\,000$.

For $20\,000 \leq Ra \leq 29\,000$, the dipole pattern transforms at first into a transitional pattern, similar to dipole smile, then into an S roll and finally it becomes a stable three-roll flow. The transition occurs without any oscillatory evolution and the energy of the final state fits the previously observed dependence between three-roll pattern energy and Rayleigh number of figure 24.

11. Summary diagrams

The energy of all stable patterns described above, as a function of Rayleigh number, is depicted on figure 29. The

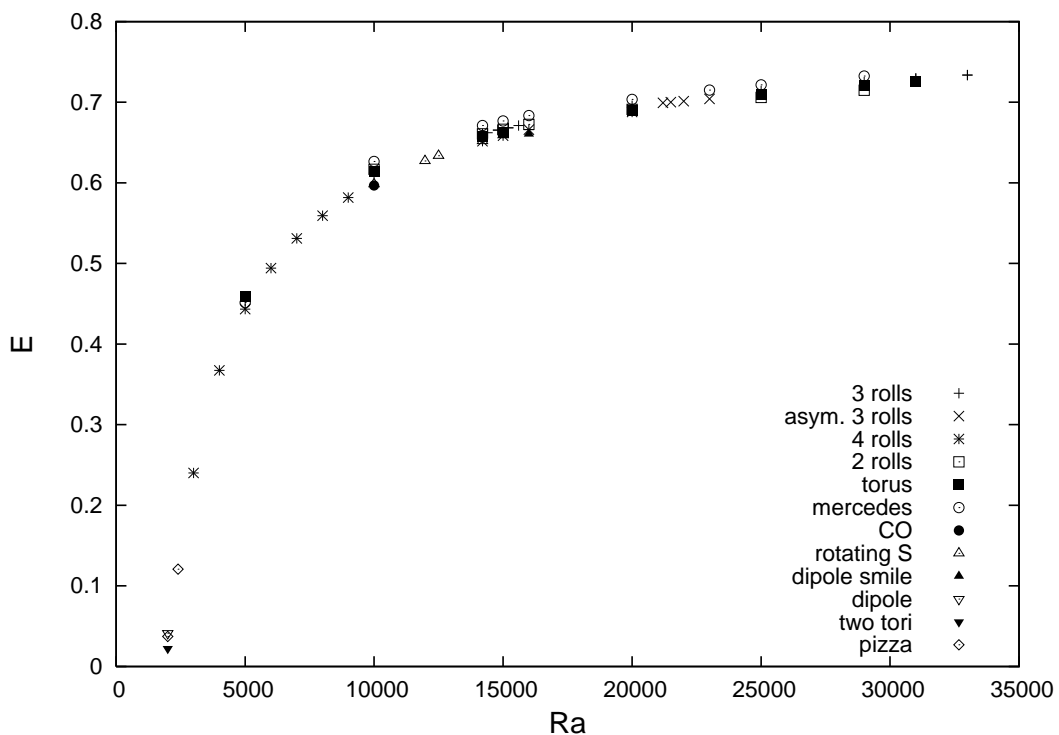


FIG. 29: Energy as a function of Rayleigh number of all stable convective patterns obtained for insulating sidewalls.

energy depends on the type of convective pattern, as well as on the Ra , but the values for different patterns obtained at the same Ra are very close.

Figure 30 shows a preliminary bifurcation diagram. We define \bar{H} to be the maximum absolute value of the temperature deviation over the ring at $(r = 0.3, \theta, z = 0)$

$$\bar{H} \equiv \max_{\theta} |H(r = 0.3, \theta, z = 0)|. \quad (12)$$

\bar{H} itself (as well as the commonly used Nusselt number) has a strong linear dependence on Ra ; plotting them directly as a function of Ra does little to separate the branches and this is why we have chosen to represent each state by its value of \bar{H}/Ra .

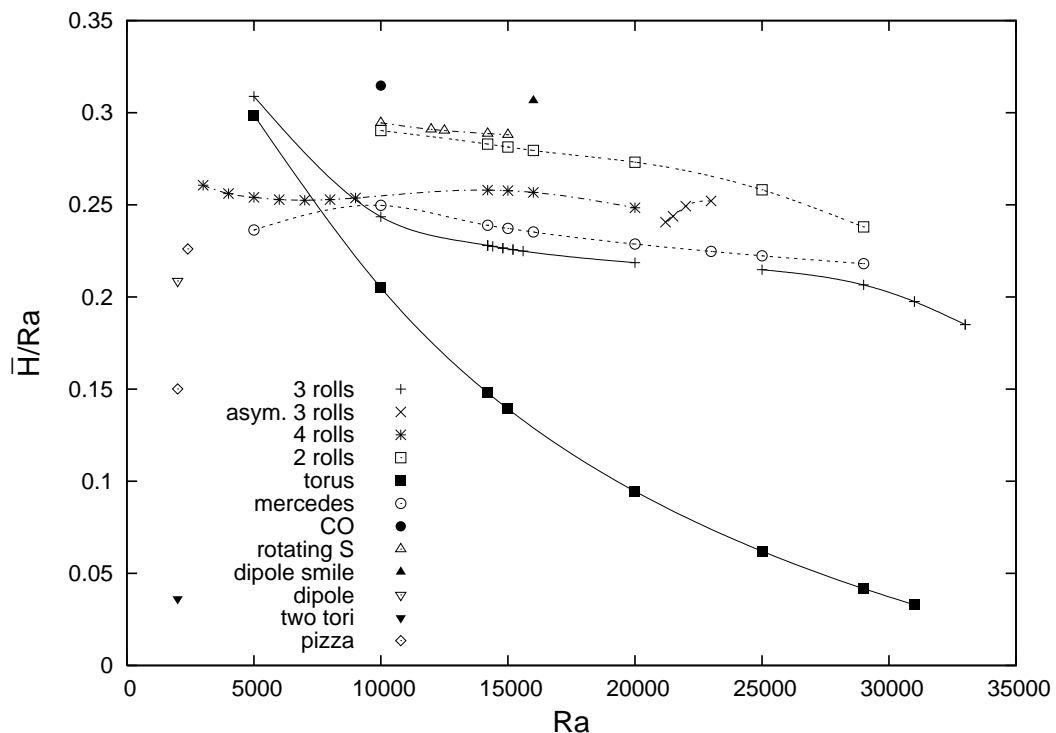


FIG. 30: Scaled temperature deviation \bar{H}/Ra as a function of Rayleigh number for all stable convective patterns obtained for insulating sidewalls.

B. Conducting sidewalls

We now present results obtained for perfectly conducting sidewalls, i.e. we apply homogeneous Dirichlet boundary conditions (3d) instead of Neumann boundary conditions (3c). The configuration is otherwise identical, i.e. $\Gamma = 2$ and $Pr = 6.7$. A schematic diagram organising all the results we will present is shown on figure 31.

1. Initialization from perturbed conductive state

As before, we initialized the first series of simulations with a perturbed conductive solution at various Rayleigh numbers between 1900 and 40 000. The initial perturbation and final states are represented symbolically on figure 31 and displayed in figure 32. For $Ra = 1900$ and 2000 the final state is of dipole form. For $2100 \leq Ra \leq 2500$, instead of the pizza pattern observed for the insulating case, we found an *hourglass* pattern, with elongated cold spots touching at the center. For $Ra = 2700$ and 4000 we obtained three rolls and for $6000 \leq Ra \leq 15000$ four rolls, which differ from the analogous patterns described previously only at the sidewalls, since, here, the deviation from the conductive profile must be zero at the boundaries. For $Ra = 20000$ we observed a *Y pattern* (figure 32g) with three bands of hot fluid in the shape of the letter Y. It is similar to the previously observed mercedes pattern, but has only one and not three symmetry axes. For $Ra = 25000$ we obtained a state in the form of a six-armed star, presented on figure 32h). For $Ra = 30000$ and above, up to 40000 , we obtained a pattern we call *da Vinci*, because of its resemblance with the artist's sketch of human body proportions (figures 32i,j). All of these flows were stationary.

2. Three rolls

In this series of simulations we used as initial condition the three-roll pattern of figure 32d. We then obtained stable three-roll patterns for a wide range of Rayleigh numbers $3000 \leq Ra \leq 24000$ and $26000 \leq Ra \leq 29000$. At $Ra = 25000$ the flow seems to evolve instead towards a two-roll state. (We can, however, obtain a three-roll pattern at

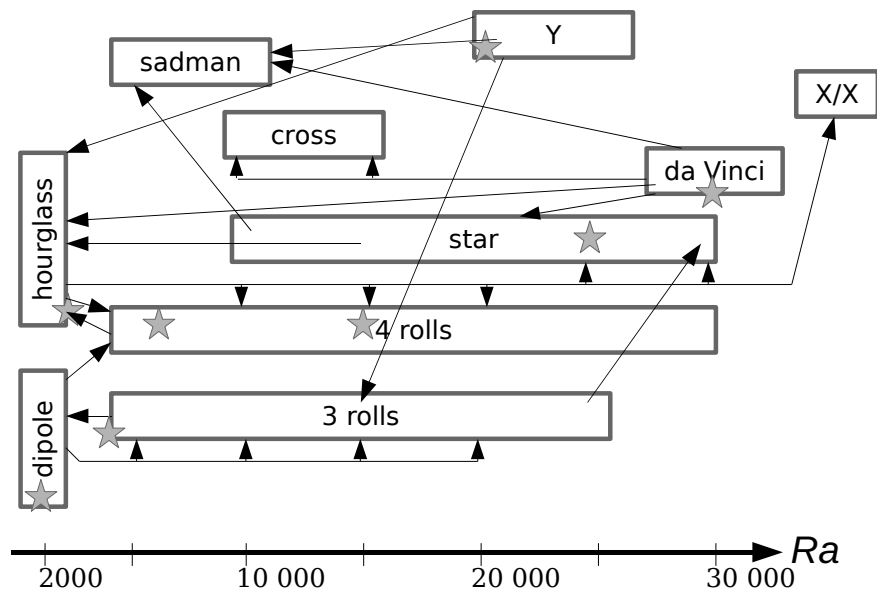


FIG. 31: Schematic diagram of stability ranges and transitions between convective patterns as a function of Rayleigh number for $\Gamma = 2$, $Pr = 6.7$ and conducting sidewalls. Stars denote solutions obtained from a slight perturbation of the conductive state, at given Ra . (see figure 32).

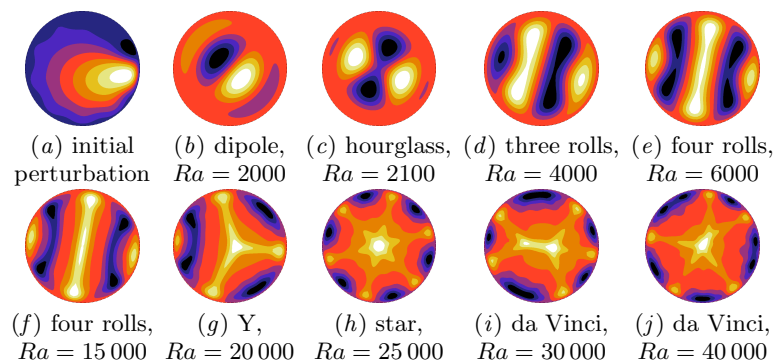


FIG. 32: Arbitrary perturbation used for initialising simulations (a) and final patterns at various Rayleigh numbers.

$Ra = 25\,000$ by initializing the simulation with three rolls obtained at $Ra = 20\,000$.) For $Ra = 30\,000$, the simulation evolves to a star pattern.

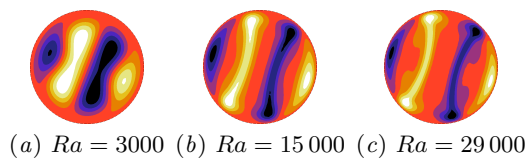


FIG. 33: Stable three-roll patterns at different Rayleigh numbers.

3. Four rolls

Every four-roll pattern we used as initial condition retained its structure within a large range of Rayleigh numbers $5000 \leq Ra \leq 35\,000$ (see figure 34). For $Ra = 2000$ the initial four-roll flow evolves into an hourglass pattern (like

that on figure 32c) and at $Ra = 40\,000$ it remains a four-roll pattern, but with the roll boundaries vibrating slightly with an oscillation period $T = 0.026$.

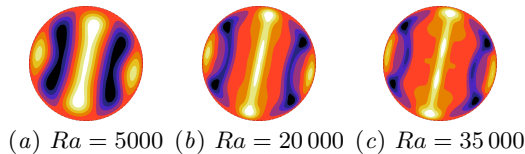


FIG. 34: Stable four-roll patterns at different Rayleigh numbers.

4. Evolution from dipole pattern

When we used the dipole pattern of figure 32b as an initial condition at higher Rayleigh numbers, the flow evolved into three rolls for $Ra = 5000$ and four rolls for $10\,000 \leq Ra \leq 20\,000$. For $Ra = 25\,000$ we obtained a Y pattern like that of figure 32g. For $Ra = 30\,000$ the simulation evolves initially towards a three-roll state, and so eventually should reach a star pattern, as ascertained in section III B 2.

5. Evolution from hourglass pattern

For simulations initialized with the hourglass pattern shown in figure 32c we obtained a stable hourglass pattern for $Ra = 2000$, four-roll flow for $5000 \leq Ra \leq 20\,000$, and a six-armed star for $Ra = 25\,000$ and $30\,000$. For $Ra \geq 35\,000$ a new standing-wave pattern appears. This state oscillates between a left-tilted and right-tilted X-letter shape, passing via intermediate star-like patterns; see figure 35. The oscillation period of this X/X state is $T = 3.05$.

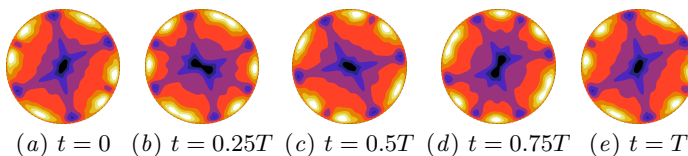


FIG. 35: Oscillatory X/X pattern at $Ra = 35\,000$.

6. Evolution from star pattern

In order to obtain patterns in the form of a six-armed star, we used as initial condition the star flow converged at $Ra = 25\,000$. Several final convective structures obtained for different Rayleigh numbers are presented on figure 36. The star flow remains stable for $10\,000 \leq Ra \leq 30\,000$ (figure 36a-b). Below this range the initial pattern evolved into a *sadman pattern* (figure 36c) at $Ra = 5000$ and an hourglass pattern at $Ra = 2000$. For both $Ra = 2000$ and $Ra = 5000$, axisymmetric transient patterns appear. For $Ra = 2000$ the transient state is composed of two concentric toroidal rolls, and its lifetime is about 30. Figure 37 shows the evolution of the energy during the transition from the initial star flow, through a long-lasting axisymmetric state into the asymptotic hourglass pattern. While the flow is axisymmetric, the energy remains almost constant.

7. Evolution from da Vinci pattern

The da Vinci pattern (figure 32i), used as initial condition, was stable only for $Ra \geq 30\,000$. For lower Rayleigh numbers the simulation evolves towards hourglass at 2000, sadman at 5000, a cross at 14 200 and 10 000 (figure 38), and a stable five-armed star at 20 000 and seemingly also at 25 000.

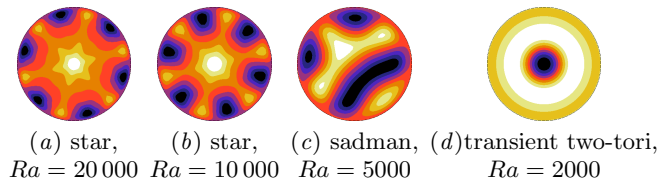
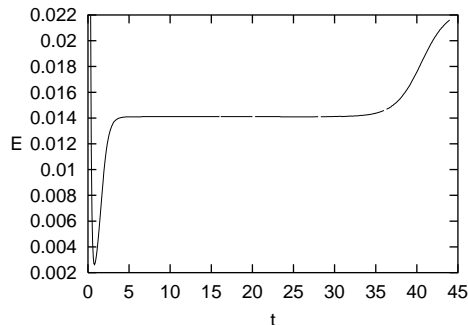
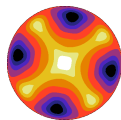


FIG. 36: Convective patterns evolved from star flow.

FIG. 37: Evolution of the system initialized with star pattern at $Ra = 2000$: energy as a function of time. Between $t = 5$ and $t = 35$ a long-lasting transient axisymmetric pattern exists.FIG. 38: Cross pattern evolved at $Ra = 10\,000$ from da Vinci flow.

8. Evolution from Y pattern

Having obtained the Y pattern at $Ra = 20\,000$ we reused it as an initial condition. We found stable Y flows for Rayleigh numbers $20\,000 \leq Ra \leq 25\,000$. For $Ra = 14\,200$ the evolution led to three rolls. For lower Rayleigh numbers we obtained sadman patterns at $Ra = 10\,000$ and $Ra = 5\,000$ and hourglass at $Ra = 2\,000$. Since there is a resemblance between the sadman and Y pattern, these may be related.

9. Summary diagrams

Figure 39 shows the energy of all stable patterns found for Dirichlet thermal boundary condition. As in the case of insulating sidewalls, the energy depends primarily on Rayleigh number, with a slight variation between types of convective patterns. Figure 40 shows \bar{H}/Ra , as defined in (12), plotted as a function of Rayleigh number, for all stable patterns found. For higher Rayleigh numbers, several patterns remain stable over large intervals of Ra : three rolls, four rolls and star. Patterns da Vinci, Y and cross were observed in smaller ranges. For lower Rayleigh numbers we observed only two stable patterns: dipole and hourglass.

IV. CONCLUSION

We have performed simulations with aspect ratio $\Gamma = 2$ and Prandtl number $Pr = 6.7$, matching the configuration of Hof *et al.* [1], who observed experimentally several different convective patterns at the same Rayleigh number. While their sidewalls were well insulating, we ran the simulations for both perfectly conducting and perfectly insulating sidewalls. The results of our simulations for insulating sidewalls are in good agreement with the experiment: we

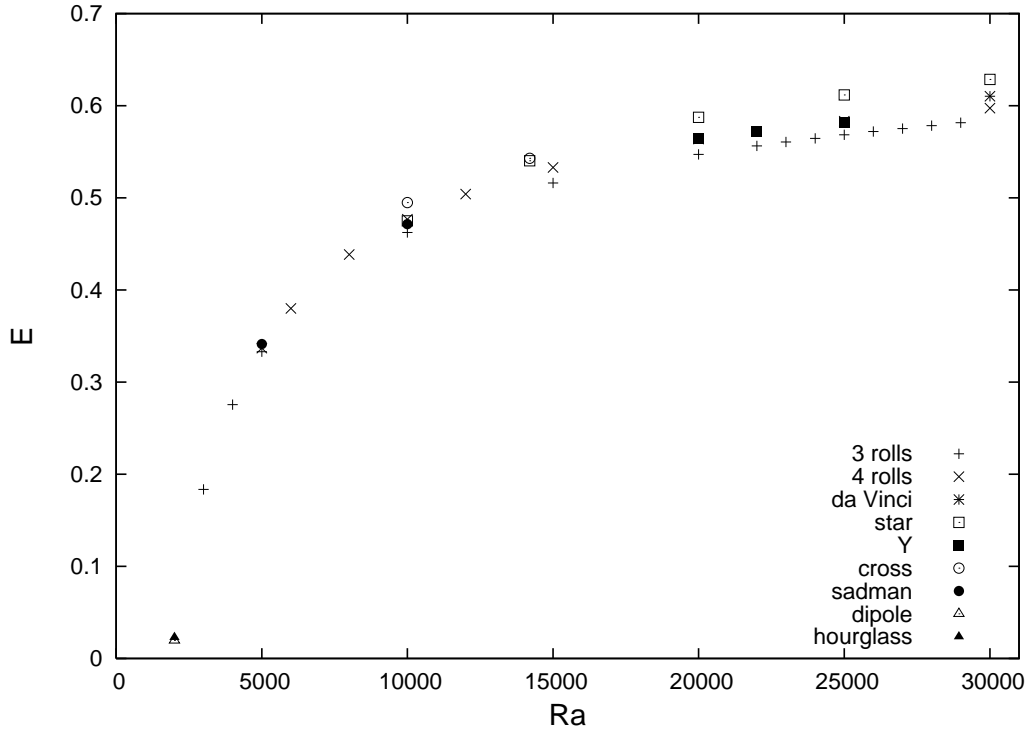


FIG. 39: Energy as a function of Rayleigh number of all stable convective patterns obtained for conducting sidewalls.

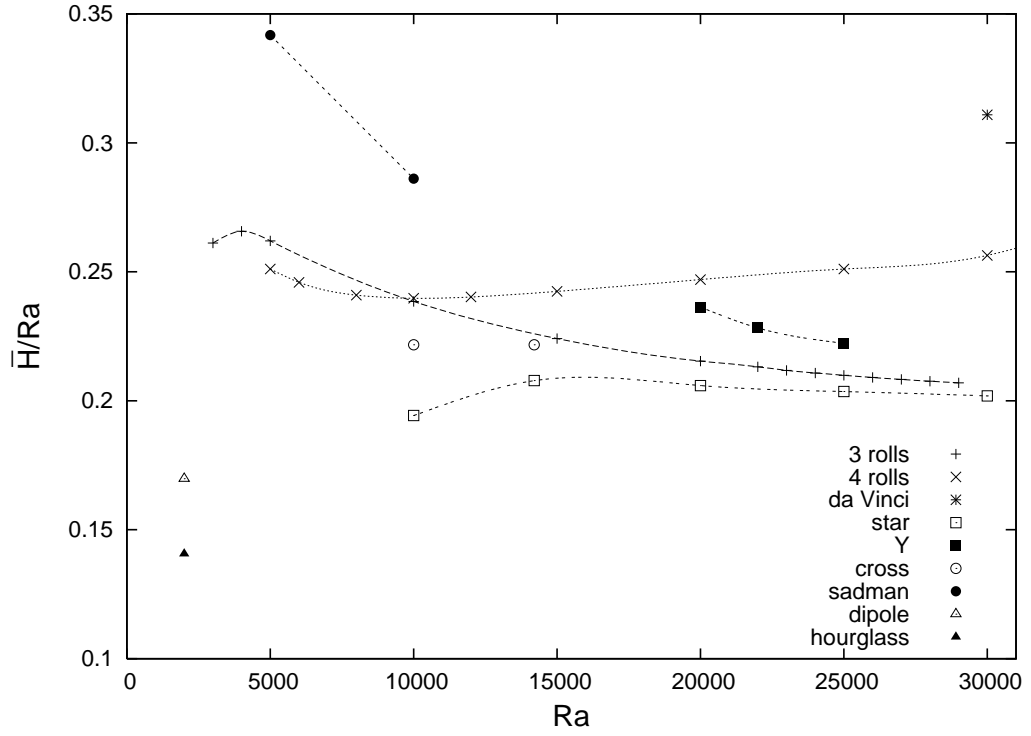


FIG. 40: Scaled temperature deviation \bar{H}/Ra as a function of Rayleigh number for all stable convective patterns obtained for conducting sidewalls.

succeeded in obtaining all five steady patterns observed experimentally for $Ra = 14\,200$. For the same Rayleigh number we observed the five stable steady solutions they reported: a toroidal roll; two, three and four parallel rolls; and a three-spoke (“mercedes”) pattern. Additionally, we obtained the rotating S structure.

For both types of boundary conditions we found multiple stable solutions for the same Rayleigh number. We preserved the nomenclature of Hof [2] and gave names to some novel patterns. We presented summary diagrams organising the complicated dependencies between the coexisting stable solutions. Our simulations confirm the fact that, even for cylinders of small aspect ratio, the form of the convective flow depends not only on Rayleigh number, but also dramatically on the initial condition. Furthermore, even for Rayleigh number as low as 2000, we found up to three different long-lived patterns.

The behaviour of the system depends both qualitatively and quantitatively on the boundary conditions. For higher Rayleigh numbers and perfectly insulating boundary conditions, among the patterns we obtain are two, three and four rolls, torus, mercedes and dipole smile. When we change the sidewalls to perfectly conducting, only three and four rolls can be observed. The axisymmetric state disappears and the mercedes state is replaced by the Y flow, thus losing its three-fold reflection symmetry. On the other hand, for conductive sidewalls, new cross, da Vinci and star flows appear. The other patterns, such as two rolls or dipole smile, may or may not also exist for conducting sidewalls. At lower Rayleigh numbers, insulating boundaries yield dipole, pizza and axisymmetric patterns. For conducting boundaries the dipole flow also exists, but the pizza pattern is replaced by hourglass and an axisymmetric pattern appears only as a transient state. In general, it seems that switching to perfectly conducting sidewalls makes some of the patterns lose their symmetries. This transition could be elucidated by performing a study in which intermediate values of sidewall conductivity would be used, and checking how the flow symmetry changes.

Close to the threshold (at $Ra = 2000$), for both types of boundary conditions, we observed different stable patterns, but none of them seem to be stable at higher Rayleigh number; conversely none of the patterns observed at higher Ra could be observed at $Ra = 2000$. In a companion paper [24], we use Newton’s method to construct a bifurcation diagram relating the states found at low Ra to those found at high Ra , for the case of insulating sidewalls. In contrast to time-stepping, Newton’s method converges more rapidly and to states regardless of their stability. The time-stepping procedure we used here lets us follow the dynamics known from the experimental scenario, including transitions between the steady and time-dependent states. The patterns we obtained have constituted a good preliminary survey for constructing a complete bifurcation diagram via continuation. This task has not yet been undertaken for the case of conducting sidewalls.

It is very likely that other stable solutions exist which we did not observe because they were topologically too far from any of our initial conditions. We observed several new time-dependent flows, but we believe that we are far from describing all existing unsteady solutions in the range of Rayleigh numbers simulated. Except for the rotating S pattern which exists for $Ra \approx 15\,000$, we observed oscillations mainly above $Ra = 30\,000$. It would also be interesting to reproduce the 13-spoke pulsing pattern found by Hof *et al.* [1] at $Ra = 33\,000$ in order to determine whether this state, evolving from axisymmetric flow, is a result of a Hopf bifurcation similar to that we described in our previous paper [33]. We showed the existence of several long-lasting transient states, for example in the case of initialization with a dipole pattern and conducting boundaries, for which the dipole smile state persisted for some time, with relatively constant energy, before transforming into the final three-roll flow. This and other transitional patterns could also be objects for further study. Despite the great variety of flows we have obtained, we are far from an exhaustive study even for this specific configuration of control parameters.

Although small-aspect-ratio cylinders lack the universality of large ones, our three-dimensional numerical study has illustrated the remarkable variety of convective flows and rich dynamics found in this system. We hope that our results convince the reader that this chapter of hydrodynamical research is not yet thoroughly written.

Acknowledgments

We gratefully acknowledge the contributions of Daniel Benaquista to this work. We thank Tom Mullin and Björn Hof for their continued interest in this work. All of the computations were performed on the computers of IDRIS (Institut pour le Développement des Ressources Informatiques et Scientifiques) of CNRS (Centre National pour la Recherche Scientifique) under project 1119.

[1] B. Hof, G. J. Lucas & T. Mullin, *Flow state multiplicity in convection*, Phys. Fluids **11**, 2815–2817 (1999).

- [2] B. Hof, *The visualisation of convective flow patterns in water in tilted cells with variable geometry*, Master's thesis, University of Manchester, 1997.
- [3] G. Charlson & R. Sani, *Thermoconvective instability in a bounded cylindrical fluid layer*, Int. Journal. Heat Mass Transfer **13**, 1479–96 (1970).
- [4] G. Charlson & R. Sani, *On thermoconvective instability in a bounded cylindrical fluid layer*, Int. Journal. Heat Mass Transfer **14**, 2157–60 (1971).
- [5] K. Stork & U. Müller, *Convection in boxes: An experimental investigation in vertical cylinders and annuli*, J. Fluid Mech. **71**, 231–240 (1975).
- [6] J. Buell & I. Catton, *The effect of wall conduction on the stability of a fluid in a right circular cylinder heated from below*, J. Heat Transfer **105**, 255 (1983).
- [7] E. L. Koschmieder, *Bénard cells and Taylor vortices* (Cambridge University Press, 1993).
- [8] F. Marques, M. Net, J. M. Massaguer & I. Mercader, *Thermal convection in vertical cylinders. A method based on potentials*, Comput. Methods Appl. Mech. Engrg. **110**, 157–169 (1993).
- [9] G. Müller, G. Neumann & W. Weber, *Natural convection in vertical Bridgeman configurations*, J. Cryst. Growth **70**, 78–93 (1984).
- [10] G. Hardin & R. Sani, *Buoyancy-driven instability in a vertical cylinder: Binary fluids with Soret effect. Part 2: Weakly non-linear solutions*, Intl J. Numer. Meth. Fluids **17**, 755 (1993).
- [11] M. Wanschura, H. C. Kuhlmann & H. J. Rath, *Three-dimensional instability of axisymmetric buoyant convection in cylinders heated from below*, J. Fluid Mech. **326**, 399–415 (1996).
- [12] R. Touihri, H. Ben Hadid & D. Henry, *On the onset of convective instabilities in cylindrical cavities heated from below. I. Pure thermal case*, Phys. Fluids **11**, 2078–2088 (1999).
- [13] D. Barkley & L.S. Tuckerman, *Traveling waves in axisymmetric convection: the role of sidewall conductivity*, Physica D **37**, 288–294 (1989).
- [14] J. H. Siggers, *Dynamics of targets in low-Prandtl number convection*, J. Fluid Mech. **475**, 357–375 (2003).
- [15] A. Pocheau, V. Croquette & P. Le Gal, *Turbulence in a cylindrical container of argon near threshold of convection*, Phys. Rev. Lett. **55** 1094–1097 (1985).
- [16] V. Croquette, *Convective pattern dynamics at low Prandtl number*, Contemporary Physics, Part I: **30**, 113–133; Part II: **30**, 153–171 (1989).
- [17] V. Steinberg, G. Ahlers & D.S. Cannell, *Pattern formation and wave-number selection by Rayleigh-Bénard convection in a cylindrical container*, Physica Scripta **32**, 534–547 (1985).
- [18] F. Busse & R. Clever, *Instabilities of convection rolls in a fluid of moderate Prandtl number*, J. Fluid Mech. **91**, 319–335 (1979).
- [19] S. Rüdiger & F. Feudel, *Pattern formation in Rayleigh Bénard convection in a cylindrical container*, Phys. Rev. E **62**, 4927–4931 (2000).
- [20] S.S. Leong, *Numerical study of Rayleigh-Bénard convection in a cylinder*, Numerical Heat Transfer, Part A **41**, 673–683, (2002).
- [21] M.R. Paul, K.H. Chiam, M.C. Cross, P.F. Fischer, H.S. Greenside, *Pattern formation and dynamics in Rayleigh-Bénard convection: numerical simulations of experimentally realistic geometries*, Physica D **184**, 114–126 (2003).
- [22] D.-J. Ma, D.-J. Sun & X.-Y. Yin, *Multiplicity of steady states in cylindrical Rayleigh-Bénard convection*, Phys. Rev. E **74**, 037302 (2006).
- [23] K. Borońska, *Three-dimensional patterns in cylindrical Rayleigh-Bénard convection*, PhD thesis, Université de Paris 7, 2005.
- [24] K. Borońska & L.S. Tuckerman, *Extreme multiplicity in cylindrical Rayleigh-Bénard convection: II. Bifurcation diagram and symmetry classification* Phys. Rev. E, submitted.
- [25] L.S. Tuckerman, *Divergence-free velocity fields in nonperiodic geometries*, J. Comput. Phys. **80**, 403–441 (1989).
- [26] D. Gottlieb & S.A. Orszag *Numerical Analysis of Spectral Methods: Theory and Applications* (SIAM, 1977).
- [27] C. Temperton, *A self-sorting in-place prime factor real/half-complex FFT algorithm*, J. Comput. Phys. **75**, 199–216 (1988).
- [28] C. Canuto, M. Y. Hussaini, A. Quarteroni & T. A. Zang, *Spectral Methods in Fluid Dynamics* (Springer-Verlag, 1988).
- [29] L.S. Tuckerman, *Transformations of matrices into banded form*, J. Comput. Phys. **84**, 360–376 (1989).
- [30] D. Rempfer, *On boundary conditions for incompressible Navier-Stokes problems*, Appl. Mech. Rev. **59**, 107 (2006).
- [31] C. Rappaport, *A color map for effective black-and-white rendering of color-scale images*, IEEE Antennas and Propagation Magazine **44**, 94–96 (2002).
- [32] B. Hof, Private communication.
- [33] K. Borońska & L.S. Tuckerman, *Standing and travelling waves in cylindrical Rayleigh-Benard convection*, J. Fluid Mech. **559**, 279–298 (2006).